SUPPORTING INFORMATION APPENDIX

Concurrent Design of Quasi-Random Photonic Nanostructures

Won-Kyu Lee,[1, †] Shuangcheng Yu,[2, †] Clifford J. Engel,[3] Thaddeus Reese,[1] Dongjoon Rhee,[1] Wei Chen,*[,2] and Teri W. Odom*[,1,3]

[1]Department of Materials Science and Engineering, Northwestern University, Evanston, Illinois 60208, USA.

[2]Department of Mechanical Engineering, Northwestern University, Evanston, Illinois 60208, USA.

[3]Department of Chemistry, Northwestern University, Evanston, Illinois 60208, USA.

[†]Authors with equal contribution.

*Corresponding authors: weichen@northwestern.edu, todom@northwestern.edu

METHODS

Preparation of PS wrinkles. PS wrinkles were formed on biaxially pre-strained, thermoplastic PS films (Grafix shrink film) by surface wrinkling.(1, 2) PS films were treated with a plasma in a reactive ion etching (RIE) system for different exposure times with the gas CHF_3 at a flow rate of 20 sccm, power of 70 W, and pressure of 20 Pa. By changing the CHF_3 time, we controlled wrinkle wavelength continuously.(3) Chemically treated PS was then heated in a convection oven at 125 °C to relieve the pre-strain of the PS substrate. The amount of strain was tuned by controlling the PS heating time. Returning the PS to room temperature stopped the shrinking process. The strain ε was determined by measuring the area of a box drawn on the substrate prior to and after shrinking and using $\varepsilon = (A_0\text{-}A_f)/A_0$, in which A_0 is the initial area and A_f is the final area. The maximum strain that can be applied to a PS film was 0.85-0.9.

Fabrication of PDMS wrinkle molds. For maximization of surface hydrophobicity, PS wrinkles were treated with an SF_6 plasma for 1 min.(2) RIE conditions (flow rate, power and pressure) for SF_6 treatment were the same as those of the CHF_3 gas. For PDMS wrinkles, we poured a mixture of pre-polymer (A/B = 1:10, Sylgard 184, Dow Corning) onto SF_6-treated PS wrinkles and cured the materials at 70 °C for 2 h.

Fabrication of quasi-random nanostructures by wrinkle lithography. An amorphous Si (*a*-Si) thin film was coated with 12-nm Al_2O_3 by atomic layer deposition (ALD). A thin film (75-150 nm) of Shipley 1805 photoresist (PR) was then spin cast on top of the Al_2O_3. The wrinkle patterns were then transferred from the PDMS stamps to the PR surfaces using solvent assisted nanoscale embossing (SANE).(4) Directional O_2 plasma in the RIE (flow rate of 50 sccm, at a power of 70 W, and a pressure of 20 Pa) reduced the thickness of the PR wrinkle patterns and exposed the underlying Al_2O_3 only in the valleys of wrinkles where the PR was thinnest. The exposed Al_2O_3

areas can be controlled by changing the O_2 plasma time to produce discontinuous PR masks with varying fill factors. Wet-etching of Al_2O_3 through the PR masks removes the exposed areas of Al_2O_3 isotropically. The etching temperature and time was fixed at 70°C and 170 s, respectively, to avoid under- and over-etching. After the wet etch, the PR masks were removed using acetone, and the 3D wrinkle structures were transferred to a 2D Al_2O_3 mask. The Al_2O_3 served as a deep reactive ion etching (DRIE) mask for etching into the Si to create the desired quasi-random pattern in 3D. For DRIE, we used CF_4 (25 sccm) and O_2 (3 sccm) gases at a power of 100 W under a pressure of 13.3 Pa.

Characterization of surface wrinkle patterns. PS wrinkles and PDMS stamps were coated with a layer of AuPd (thickness ca. 8 nm) for SEM imaging. Quasi-random structures at each stage of wrinkle lithography was imaged with SEM (without coating of AuPd) and tapping-mode atomic-force microscopy (AFM). The broadband absorbance spectra on quasi-random *a*-Si patterns were measured from 400 to 1200 nm using a LAMBDA 1050 spectrophotometer (PerkinElmer) or Cary 5000 UV− vis−NIR spectrophotometer (Agilent Technologies).

SDF-based representation of quasi-random structures. The spectral density function (SDF) was used to represent and model the quasi-random nanostructures formed by wrinkle lithography. The underlying mathematical correlations between the structural spatial functions of the patterns and their Fourier spectrum have been well established based on the Winner-Khinchin theorem.(5) Therefore, SDF calculated from the Fourier spectrum can describe the degree of order versus disorder of the quasi-random structures in the spatial frequency (k) domain.(6) Since typical SDFs have less than four characteristic parameters, the SDF-based structural representation significantly reduces design dimensionality, which allow fast explorations of optimal quasi-random nanostructures. For example, following equation characterizes the SDF of the 3D morphology

formed in micro-emulsions of oil, water and surfactant:(7)

$$p(k) = C \cdot \left[\left(k^2 + k_0^2 \right) \cdot \left(k^4 + 2k^2 b^2 \cos 2t + b^4 \right) \right]^{-\frac{1}{2}}$$

Three parameters, i.e. k_0, b, and t governs this SDF ($p(k)$) with C as the normalization constant. Usually, the governing parameters of SDF associate with physical properties of the structures in real-space. For instances, in this system, the length scale is set by $(\mathbf{E}[k^2])^{1/2} = (b^2+2bk_0\cos t)^{1/2}$ where $\mathbf{E}[\bullet]$ denotes the mean value. The minimum feature size is determined by the value of k as $p(k)$ converges to zero and the main quasi-periodicity is determined by the value of k that maximizes $p(k)$. These physical properties that are usually determined by the fabrication processing conditions would affect the functional performances of the structure. Therefore, the SDF representation of quasi-random nanostructure bridges the gap in process-structure and structure-performance relations, and provides the foundation for concurrent design of the structure and fabrication conditions.

Genetic algorithm for optimization search. We used genetic algorithm (GA) to update the structural parameters of wrinkle patterns in the iterative search of the optimal solution. Mimicking natural evolution with the underlying idea of survival-of-the-fittest, GA is a stochastic, global search algorithm.(8) The stochasticity of GA enables the convergence toward optimums despite the strong design nonlinearity (i.e., the existence of large numbers of local optimums) in nanophotonic optimization problems.(9, 10) However, GA is usually inefficient to solve the structural optimization problems due to the large numbers of design variables, especially, for the case of pixelated representation.(11) We overcame this problem by using SDF-based representation for the nanowrinkle patterns, which depends only on three variables of λ, f and t. The variables were coded using the binary notation and were regarded as the chromosomes in GA.

A population of the chromosomes went through the iterative operation of selection, recombination, and mutation and converged to the optimized broadband, light trapping structure.

Although GAs with different strategies of selection, recombination, and mutation have been developed, we used the strategy of self-adaptive mutation.(12) Here, the designs mutate by adding a random parameter with normally distribution to each design variable. The mutation strength (i.e., standard deviation of the normal distribution) was self-adaptive and varied during the optimization process. The strength increased as the optimization converged. We observed this self-adaptive control of the mutation in the history plot (Fig. 4A) where larger fluctuations occurred at the late stage of the optimization (converged regime, number of evaluations = 186) compared to the beginning stage (linear regime, before 130^{th} evaluation). In this work, the self-adaptive GA search was performed using the commercial optimization software *iSight* from *Dassault Systemes.*

Finite-difference time-domain simulation. Finite-difference time-domain (FDTD) calculations based on commercial software (FDTD Solution, Lumerical Inc., Vancouver, Canada) were used to simulate the light-trapping performance and the near-field distribution of optimized *a*-Si nanostructures (λ = 550 nm, f = 52%, t = 210 nm) in a 3 μm × 3 μm window. The total thickness of the *a*-Si slab was set as T = 700 nm on top of the silver backing layer. To ensure no transmission though the system, we set the thickness of the Ag layer as 300 nm. A uniform mesh size of 6 nm (x, y and z directions) was used to improve the spatial resolution of the fields. The simulation had periodic boundary conditions in the x-y direction and a perfectly matched layer (PML) in z. The frequency dependent real and imaginary dielectric constants for amorphous silicon were taken from reference. (13)

Formation of Al_2O_3 quasi-random pattern on *a*-Si substrate

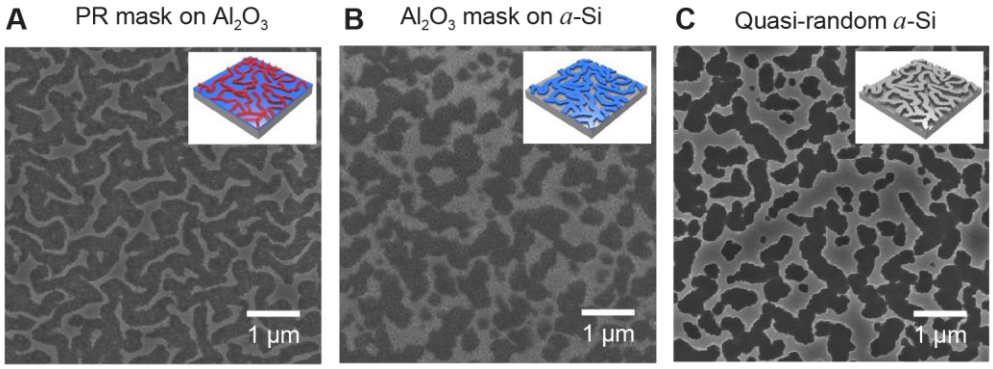

Fig. S1. Formation of two-dimensional, quasi-random Al_2O_3 mask on *a*-Si substrate. SEM images of **(A)** quasi-random PR mask on Al_2O_3 surface before wet-etching, **(B)** quasi-random Al_2O_3 mask on the surface of *a*-Si after wet-etching and lift-off the PR mask, **(C)** quasi-random *a*-Si pattern in 3D after DRIE and subsequent etching of the Al_2O_3 mask.

Rigorous coupled wave analysis of broadband light-trapping device

We evaluated the light absorption (*A*) of the nanowrinkle pattern using:

$$A(\varepsilon) = \frac{I - R(\varepsilon) - T(\varepsilon) - D(\varepsilon)}{I} \quad \text{(S1)}$$

where *I* is the incidence, *R* and *T* are the zeroth-order reflection and transmission respectively, *D* denotes the deflected higher order reflection and transmission, and $\boldsymbol{\varepsilon}$ represents the permittivity distribution. Predicting the light absorption of the structure requires calculation of the interaction between electromagnetic wave and the system, for which we used a stable Rigorous Coupled Wave Analysis (RCWA) method developed in literature.(14-16) This method obtains the exact solution of Maxwell's equations for the electromagnetic diffraction by grating structures. Moreover, the algorithm has the advantages of good convergence and relatively simple implementation for analyzing periodic structures by only considering a unit cell with infinite-repeating boundary conditions. RCWA has been applied in the analysis of various systems, such as metal-dielectric multilayer structures(17) and nanowire enhanced biosensors.(18)

To analyze the reflection, transmission and deflection through a multilayered dielectric stack using RCWA, Fourier expansions of electric, magnetic field and the permittivity were made to achieve an algebraic eigenvalue system for each layer.(15, 19) In the simulation of our quasi-random light-trapping structures, we assume that there is no geometric variation in the vertical direction of the wrinkle patterns. Thus, the system of light-trapping device consists of three layers: (1) wrinkle patterned *a*-Si, (2) *a*-Si thin-film without the pattern, and (3) Ag layer at the bottom. The orders of Fourier components considered in each analysis determine the accuracy of the results. Although higher orders of Fourier components can lead to more accurate transmission and reflection, the computation time increases significantly. Here, an order of 21 was selected by considering the trade-off between calculation accuracy and speed. Assuming the scattering layer

is discretized by a *N*-by-*N* grid mesh, we can calculate the Fourier components of the permittivity by:

$$\varepsilon\left(k_x,k_y\right)=\frac{1}{N_x\times N_y}\sum_{i=1}^{N_x}\sum_{j=1}^{N_y}\varepsilon\left(x_i,y_j\right)e^{-i\cdot\left(k_x x_i+k_y y_j\right)} \tag{S2}$$

Solving the eigenvalue problem in each layer results in the so-called scattering matrix (S matrix, **Fig. S2**), and the S matrix for the entire multi-layer system can be obtained by:

$$S=S_1\times S_2\times\cdots S_n \tag{S3}$$

Input [A_1, B_1] and output [A_2, B_2] are related by the Poynting's theorem:

$$\begin{bmatrix}A_1\\B_1\end{bmatrix}=S\times\begin{bmatrix}A_2\\B_2\end{bmatrix} \tag{S4}$$

Therefore, the obtained B_1 and A_2 vectors yield *R*, *T* and *D* of the multi-layer system in **Equation S1**.

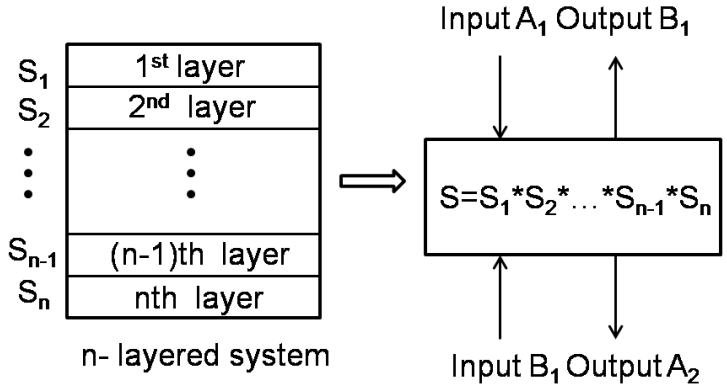

Fig. S2. Schematic illustration of RCWA algorithm for multi-layered system

We note that RCWA assumes a periodic boundary condition over the input structure (the unit cell). In our calculation, we set the length of the unit cell structure as 3000 nm. Since SDF provides information regarding the distribution of spatial frequency of the structure, different real-space

structures reconstructed from the same SDF are statistically equivalent in reciprocal space. The characteristics of the reciprocal space of the structure determine their performance for photon management.(20) Therefore, the light-trapping performance of a quasi-random structure consisting of statistically equivalent unit cells with different real-space geometries is theoretically the same as that of a structure as a periodic arrangement of the same unit cell.

Process-Structure mapping

Design of quasi-random nanostructures from wrinkle lithography is defined by three variables, wrinkle wavelength (λ) that determines SDF, materials filling ratio (f), and feature depth (t). We can control these three parameters independently by varying the fabrication processing conditions: CHF_3 time (t_{CHF3}) for λ, O_2 etching time (t_{O2}) for f, DRIE time (t_{DRIE}) for t. We obtained the linear relation of the process-structure mapping for each pair of structure-processing parameters from the data in **Fig. S3**. **Equations S5** show mathematical expressions of the linear fittings. From the process-structure mapping, we can identify combinations of processing conditions (t_{CHF3}, t_{O2}, t_{DRIE}) for a given nanostructure design, which enables concurrent design of structure and processing.

$$\begin{cases} t_{CHF3} = 0.2087 \cdot \lambda - 37.5758 \\ t_{O2} = -36.86 \cdot f + 71.63 \\ t_{DRIE} = 0.325 \cdot t - 2.7451 \end{cases} \quad \text{(S5)}$$

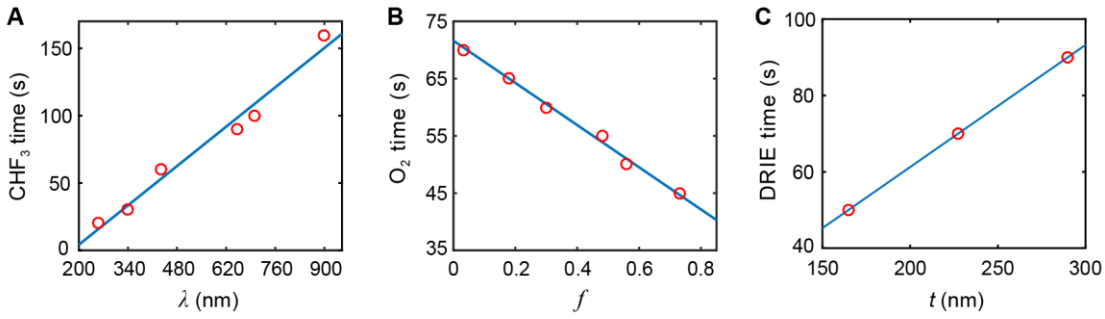

Fig. S3. Process-structure mapping in wrinkle lithography. Linear relations of **(A)** wrinkle wavelengths (λ) and CHF_3 time, **(B)** O_2 etching time and material filling ration (f) and **(C)** DRIE time and the thickness of *a*-Si patterns.

Comparison of SDFs from PDMS and *a*-Si wrinkle patterns

We confirmed that the degree of order versus disorder of the nanowrinkle pattern on PDMS stamp was preserved in the final patterned structure on *a*-Si by analyzing the corresponding SDFs. **Fig. S4A-B** show binarized SEM images of the PDMS wrinkle and the *a*-Si pattern. Using the corresponding Fourier spectra, we obtained the normalized SDFs for comparison (**Fig. S4C**). The SDFs from the PDMS stamp and *a*-Si pattern matched well with each other, indicating that the quasi-random patterns were successfully transferred from the template to target material.

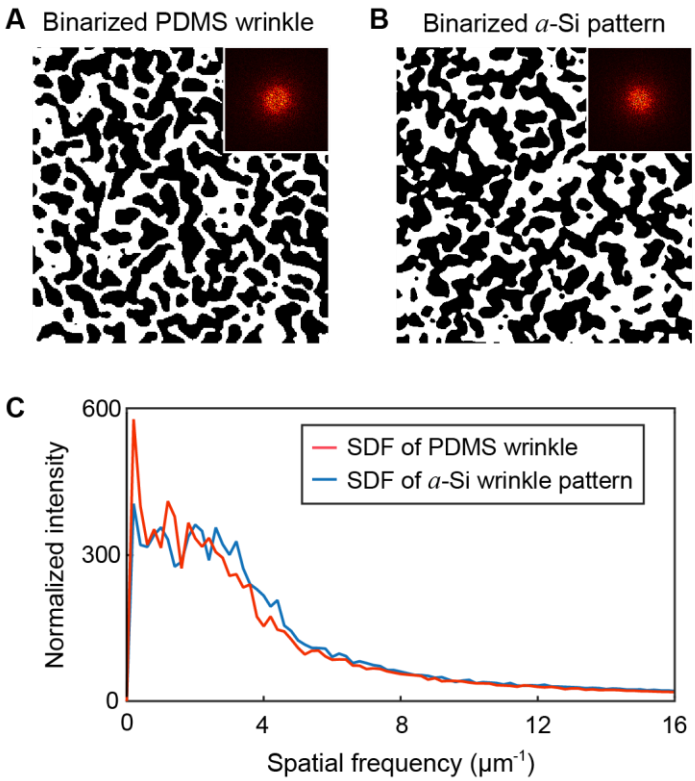

Fig. S4. SDF-based analysis of the preservation of degree of order/disorder during wrinkle lithography. Binarized SEM images of **(A)** PDMS wrinkle stamp and **(B)** resulting *a*-Si pattern by wrinkle lithography. **(C)** SDFs from the images in (A) and (B).

Truncated Gaussian distribution function as a SDF of multiscale wrinkle patterns

We analyzed wrinkle patterns with different wavelengths ranging from 180 nm to 2000 nm using the SDF formulation. We numerically derived that SDFs $p(k)$ of the quasi-random patterns in *a*-Si followed a hill shape truncated from a Gaussian distribution function. Here, both mean (μ) and standard deviation (σ) of this Gaussian distribution function depended on wrinkle wavelength (λ) as $\mu = k_m = 1/\lambda$ and $\sigma = 0.958/\lambda + 0.00017$ where the *r*-square (coefficient of determination) for the fitting was 0.98. **Fig. S5** shows SDF fitting results for different λ of 180 nm, 450 nm, 650 nm and 2000 nm.

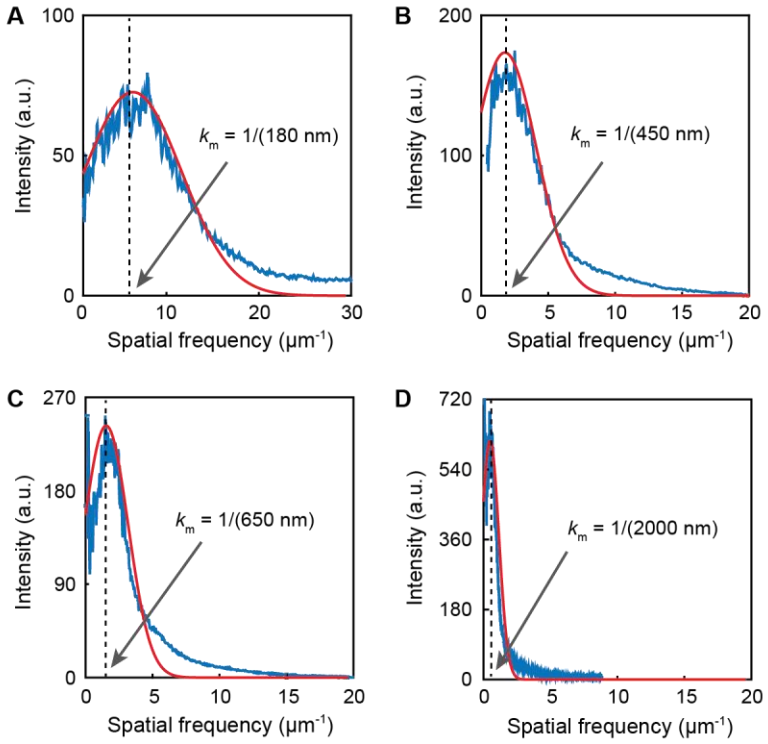

Fig. S5. Fitting results of the SDFs of *a*-Si quasi-random patterns having different wavelengths. SDFs follows truncated Gaussian distribution functions for wrinkle wavelength of **(A)** 180 nm, **(B)** 450 nm, **(C)** 650 nm and **(D)** 2000 nm. The blue curves denote the measured SDFs and the red curve show the fitted truncated Gaussian distribution functions.

Reconstruction of SDFs using Gaussian random field modeling

Reconstruction of SDFs is necessary for structure-performance simulations in the iterative optimization process. We developed a method based on Gaussian random field (GRF) modeling to reconstruct nanowrinkle patterns in real-space based on SDF representation. A standard GRF ($Y(\mathbf{r})$) is a random field with each point $\mathbf{r}$ marginally following a standard Gaussian distribution. The GRF over a n-dimensional space is completely governed by the field-field correlation function $g(\mathbf{r}_1, \mathbf{r}_2)$ in **Equation S6**.

$$g\left(\mathbf{r}_1,\mathbf{r}_2\right)=\mathbf{E}\left[Y(\mathbf{r}_1)Y(\mathbf{r}_2)\right]=\int_0^\infty \frac{J_{(n-2)/2}\left(k\Delta r\right)}{\left(k\Delta r\right)^{(n-2)/2}}\cdot k^{n-1}\cdot p^2(k)dk,\quad \Delta r=\left|\mathbf{r}_1-\mathbf{r}_2\right| \tag{S6}$$

$$Z\left(\mathbf{r}\right)=\begin{cases}1, & Y(\mathbf{r})\le\alpha\\ 0, & Y(\mathbf{r})>\alpha\end{cases} \tag{S7}$$

Defined as the statistical correlation between two points over the random field, $g(\mathbf{r}_1, \mathbf{r}_2)$ describes fluctuation characteristics of the GRF. In **Equation S6**, J are Bessel functions of the first kind, and $p(k)$ is the spectral density function (SDF). **Equation S6** shows the analytical relationship between GRF $Y(\mathbf{r})$ and SDF $p(k)$. Once GRF is generated, we can obtain the quasi-random structure in real-space dictated by $Z(\mathbf{r})$ (**Equation S7**) by level-cutting GRF $Y(\mathbf{r})$ at α, whose value is determined by desired material filling ratio. **Fig. S6** illustrates the reconstruction process based on a delta-function (**Fig. S6A**) as SDF. A GRF is first constructed based on this targeting SDF. After level-cutting the random field by 50% material filling ratio, we achieved the reconstruction in real-space (**Fig. S6C**). We confirmed that the Fourier spectrum of the reconstruction (inset) matches with the original SDF.

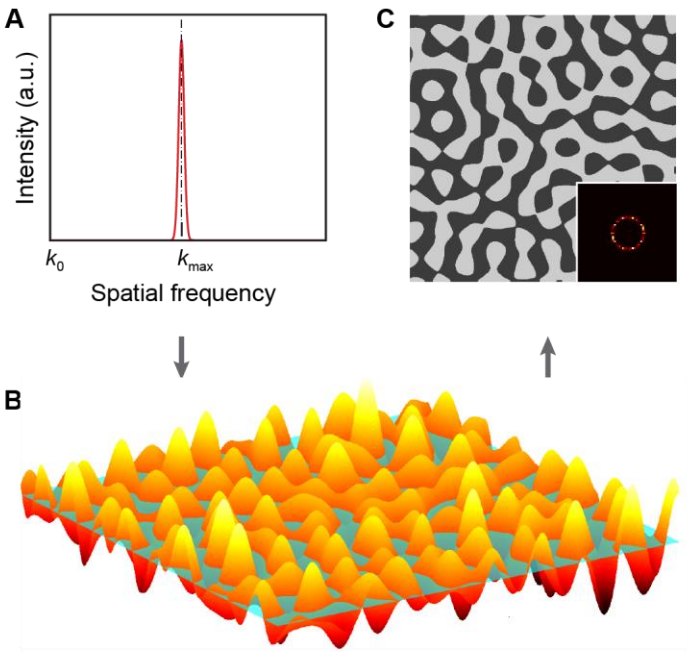

Fig. S6. Real-space quasi-random structure reconstruction based on SDF using Gaussian random field modeling. (A) Delta function as a sample SDF. **(B)** Gaussian random field. **(C)** Reconstructed structure in real-space.

Fig. S7 demonstrates the capability of the GRF-based method to reconstruct various real-space structures to target different SDFs. **Fig. S7A** shows the reconstruction process of SDF which follows a truncated Gaussian distribution. The reconstructed structure in real-space with the material filling ratio of 60% shows a Fourier spectrum (inset) corresponding to the target SDF. **Fig. S7B** depicts the case of an SDF that has a two-step shape. Here, the material filling ratio was set at 50% and the reconstructed structure possessed a double-band Fourier spectrum matching the target SDF. Lastly, the three-delta SDF in **Fig. S7C** produced the reconstruction with a triple-ring Fourier spectrum. The material filling ratio was set as 40% for this case. Based on these case studies, we conclude that our reconstruction method can deal with SDFs of arbitrary forms including quasi-random wrinkle patterns showing SDF with truncated Gaussian distribution.

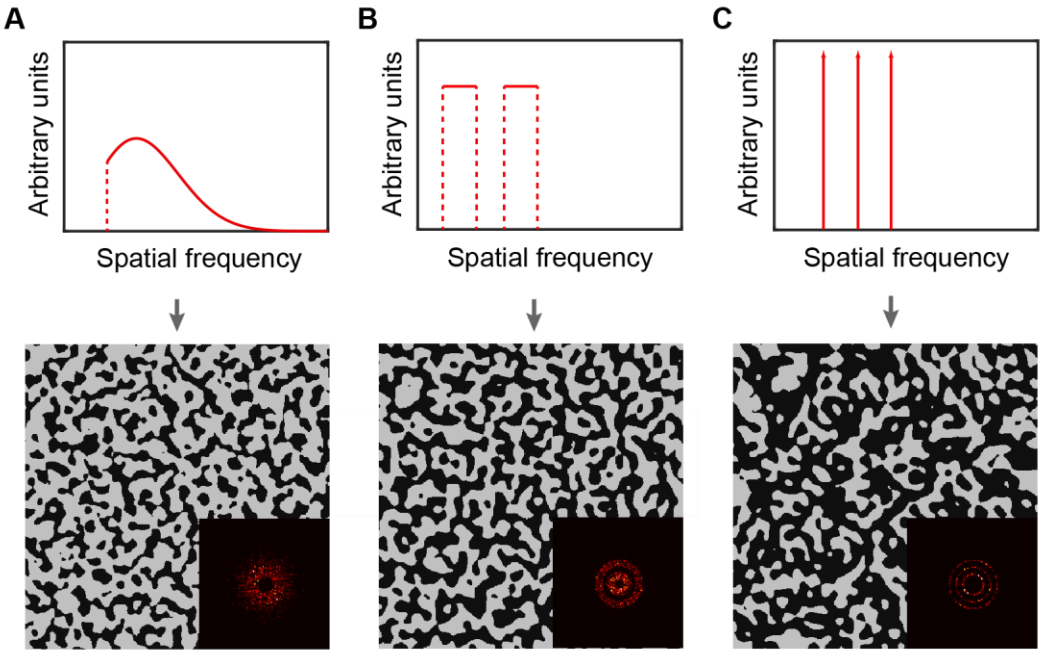

Fig. S7. Real-space quasi-random structure reconstruction using Gaussian random field modeling for different forms of SDFs. Reconstruction of SDFs following **(A)** truncated Gaussian distribution, **(B)** two-step shape, **(C)** three-delta function.

Broadband light trapping on quasi-random nanostructures with identical SDF

Quasi-random structures with different real space geometries but very similar Fourier spectrums originating from the same SDF showed the same absorption performance. **Figure S8** highlights an optimized quasi-random light-trapping structure using the SDF-based representation and reconstruction. Here, the thickness of the quasi-random light- trapping structure (t_1) was set as 100 nm, and the total thickness of *a*-Si layer was set as 600 nm. The light-trapping nanostructure was optimized under normal-incidence light of 650 nm. We assumed that the quasi-random

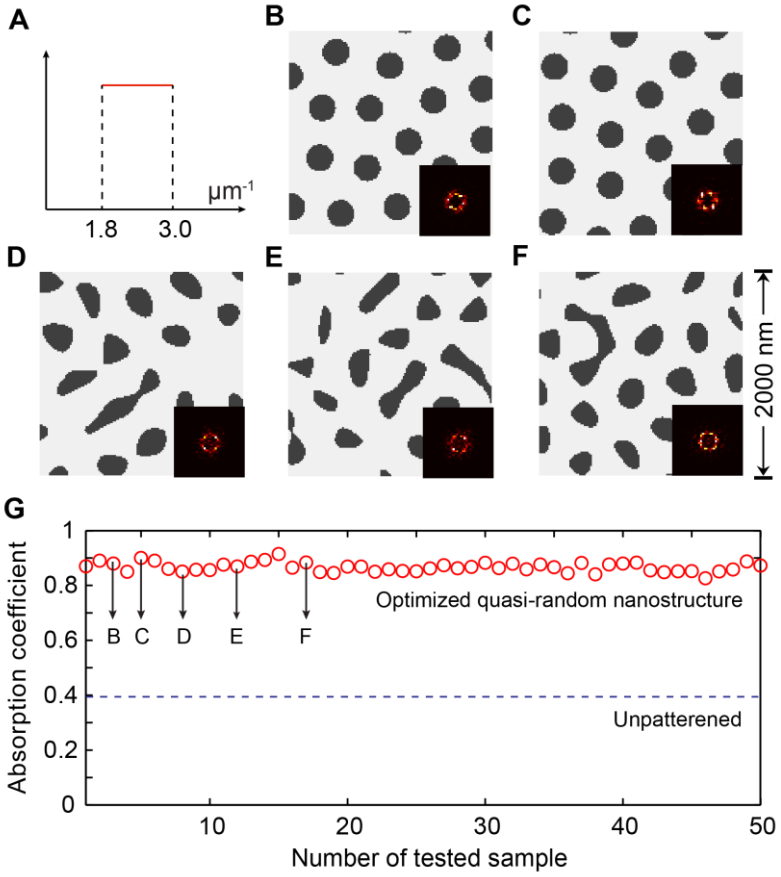

Fig. S8. SDF based design of quasi-random light-trapping structures. (A) Optimized step-shaped SDF for light-trapping nanostructures. **(B, C)** Real-space structures reconstructed from the optimized step-shaped SDF using random disk packing algorithm. **(D, E, F)** Real-space structures reconstructed from the optimized step shaped SDF using Gaussian random field modeling. **(G)** RCWA absorption performance validation of 50 different structures reconstructed from the optimized step shaped SDF.

structures follow a step shaped SDF shown in **Fig. S8A** governed by the spatial frequencies on the two ends. These two frequencies with the material filling ratios of the structure were optimized for maximal light absorption. The optimized step shaped SDF shown in Fig. S8A starts at 1.8 μm^{-1} and ends at 3 μm^{-1} with the material filling ratio of 78%. Based on this solution, five designs with different real-space geometries were reconstructed at 2 μm-by-2 μm scale; the structures in the **Fig. S8B-C** were generated using random disk packing method, and the structures in the **Fig. S8D-F** were generated using Gaussian random field modeling. Despite different real-space morphologies, all designs showed similar ring-shaped Fourier spectra and achieved equally optimized light-trapping performance. Including these five samples, 50 different real-space patterns were generated from the optimized SDF, and evaluated using RCWA. **Figure S8G** shows that the designs achieved an average absorption of 0.88, a 225% enhancement compared with the unpatterned cell. There is less than 4% variance of the absorptions of these designs. From this test case, we confirmed that structures with different real space geometries and the same SDF can achieve similar absorption performance.

Broadband optimization of average absorption enhancement factor

Broadband optimization maximizes the average absorption enhancement factor, defined as the ratio between the predicted absorption and the single-path absorption averaged over different wavelengths (**Equation S8**).

$$\sum_{w_i}^{w_n} \frac{A(\mathbf{Z}, w_i)}{A_S(w_i)} \Big/ n \tag{S8}$$

In this equation, $A(\mathbf{Z}, w_i)$ denotes the absorption of the structure **Z** at incident wavelength w_i evaluated by RCWA, and $A_S(w_i)$ denotes the single-path absorption at incident wavelength w_i. (21, 22) Here, the absorption enhancement factor describes the light-trapping efficiency of the quasi-random wrinkle patterns. **Fig. S9** shows the enhancement factor of the initial design and the optimized design in the weak absorbing spectrum of *a*-Si. Notably, the structural optimization increased the averaged enhancement factor from 1.6 to 4.7 as confirmed in the optimization history plot (Fig. 4A).

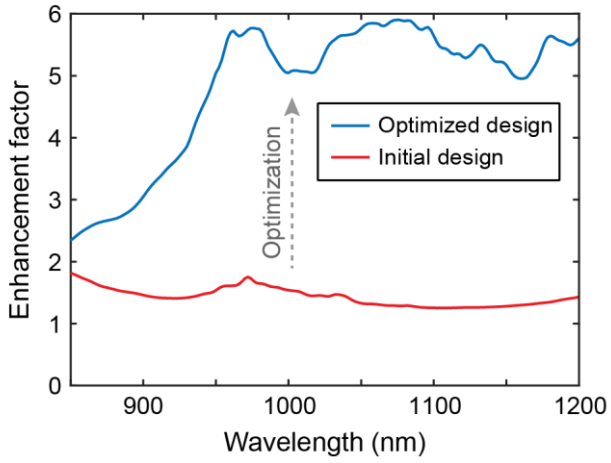

Fig. S9. Absorption enhancement factor of the initial design and optimized design of nanowrinkle patterns.

Evolving process of structural parameters during broadband optimization

Due to the self-adaptive control of mutation strength (**Methods**), the values of the three design variables fluctuated during the broadband optimization (**Fig. S10**). We observed that the fluctuation increased after the optimal design was identified. As the optimization is approaching the convergence, the level of fluctuation increased due to the increased mutation strength controlled by the self-adaptive mutation. Such a strategy reduces the likelihood of the optimization being trapped at a local optimum with relatively low performance.

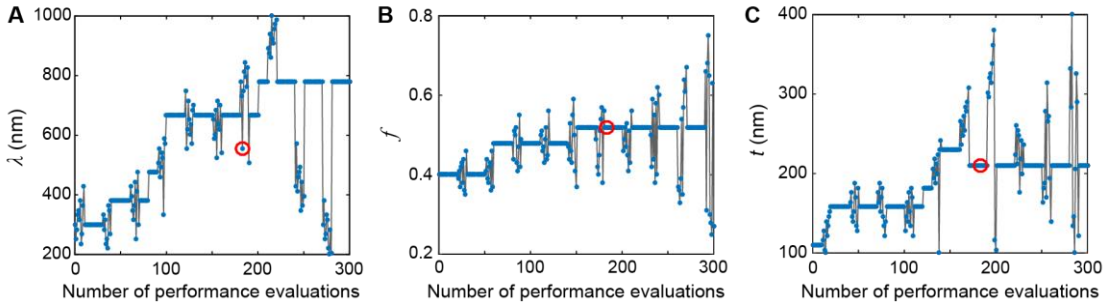

Fig. S10. Optimization history plot for different structural parameters. (A) Wrinkle wavelength (λ), **(B)** material filling ratio (f) and **(C)** feature depth (t) as a function of performance evaluation numbers. The red circle in the plots denotes the optimized solution.

SDFs of local areas on wafer-scale optimized quasi-random nanostructures

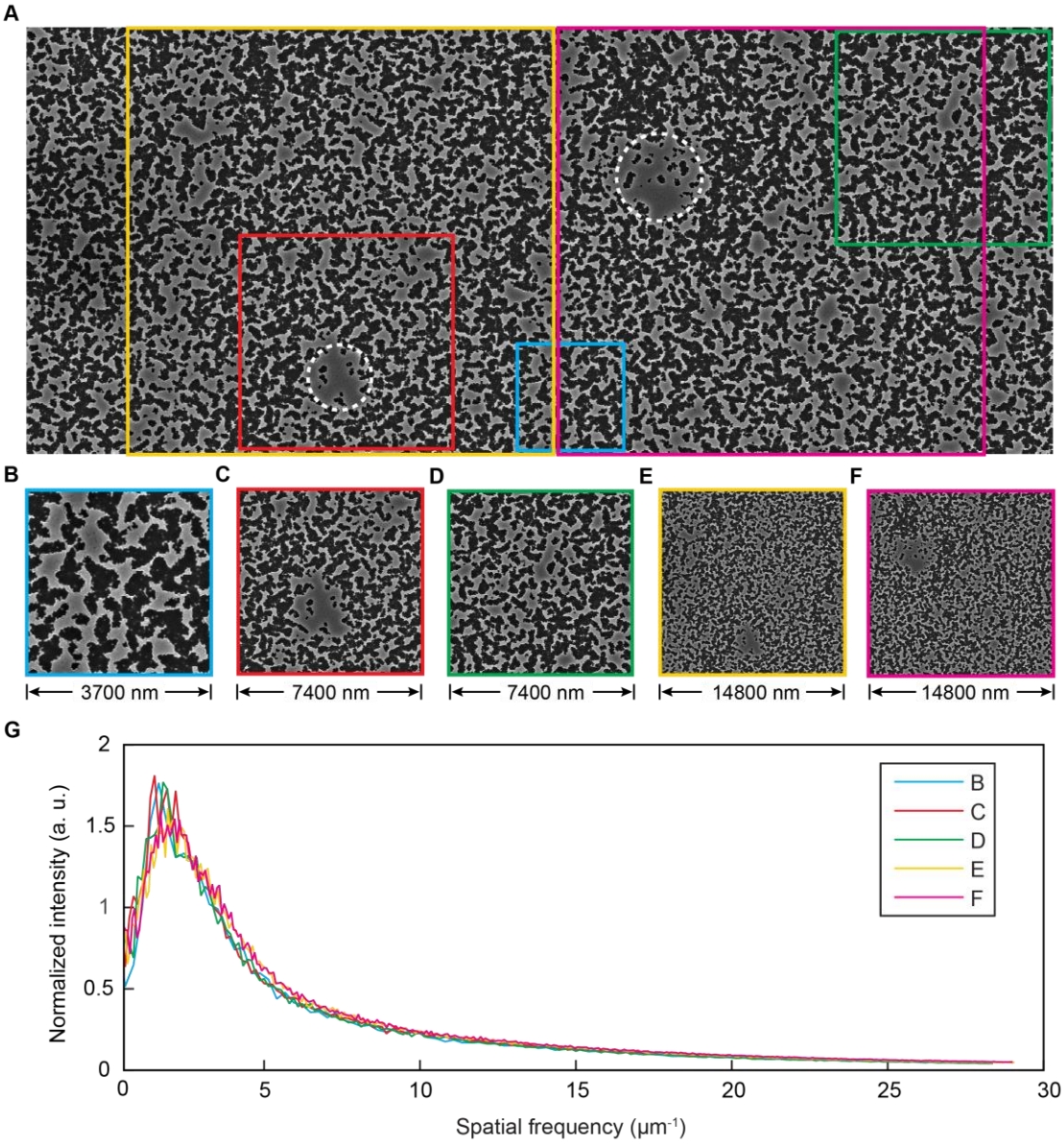

Fig. S11. SDF analysis of different local areas from the optimized quasi-random *a*-Si structure. (A) SEM images of large-area, quasi-random structure on *a*-Si film consisting of different local structures. **(B-F)** Five local patches of from the quasi random pattern in (A). **(G)** The calculated SDFs of the structures in (B-F) are plotted for comparison. Local patches with different colored boxes in (A) correspond with those in (B-F). Dotted circles in (A) show local defects formed by wrinkle lithography.

Calculation of near-filed distribution by finite-difference time-domain (FDTD) simulations

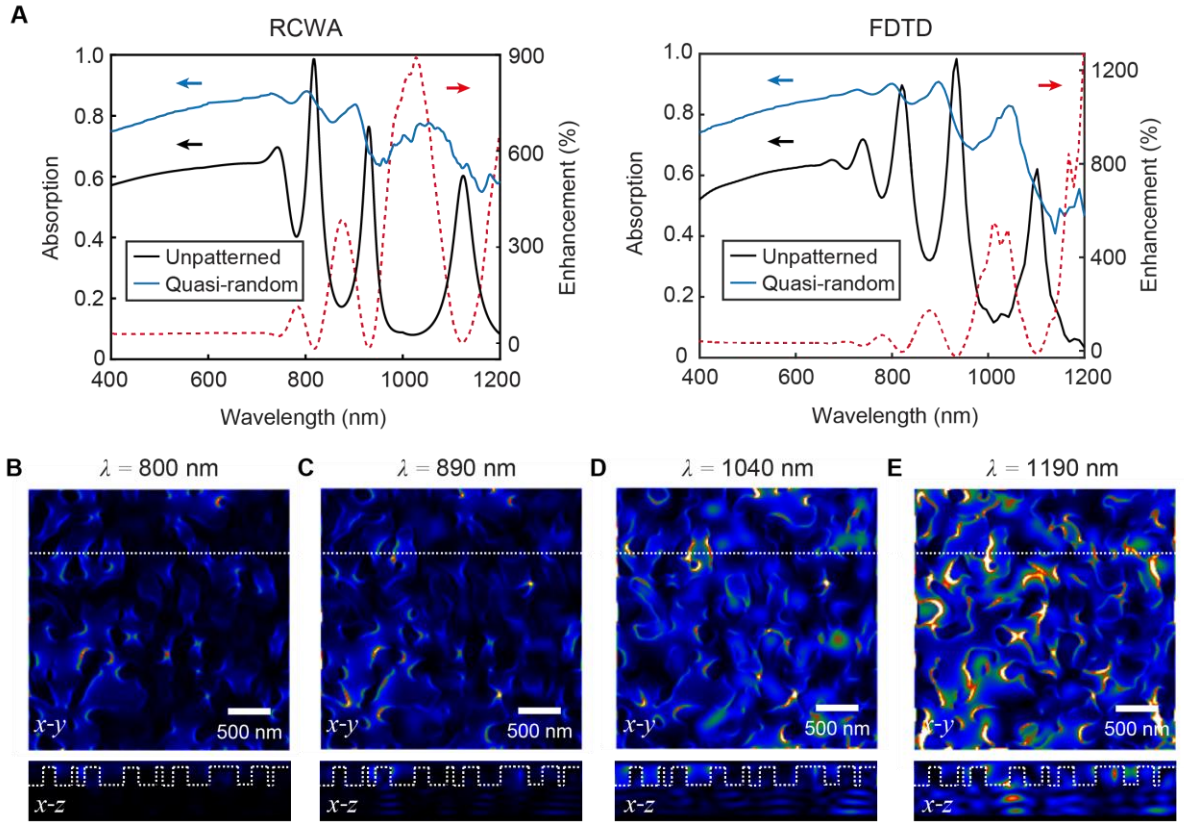

Fig. S12. Broadband, light-trapping on quasi-random *a*-Si structure simulated by FDTD. **(A)** Absorption spectrum of the optimized structure in Fig. 4B calculated by RCWA (left) and FDTD (right). Calculated near-field intensity profile (top and side views) obtained at a light wavelength **(B)** λ = 800 nm, **(C)** λ = 890 nm, **(D)** λ = 1040 nm and **(E)** λ = 1190 nm. The normalization on the color scale is made with respect to the highest value of wavelength λ = 800 nm for direct comparison. The side field profiles correspond with the dot lines in the top images.

Additional surface roughness on the quasi-random *a*-Si patterns

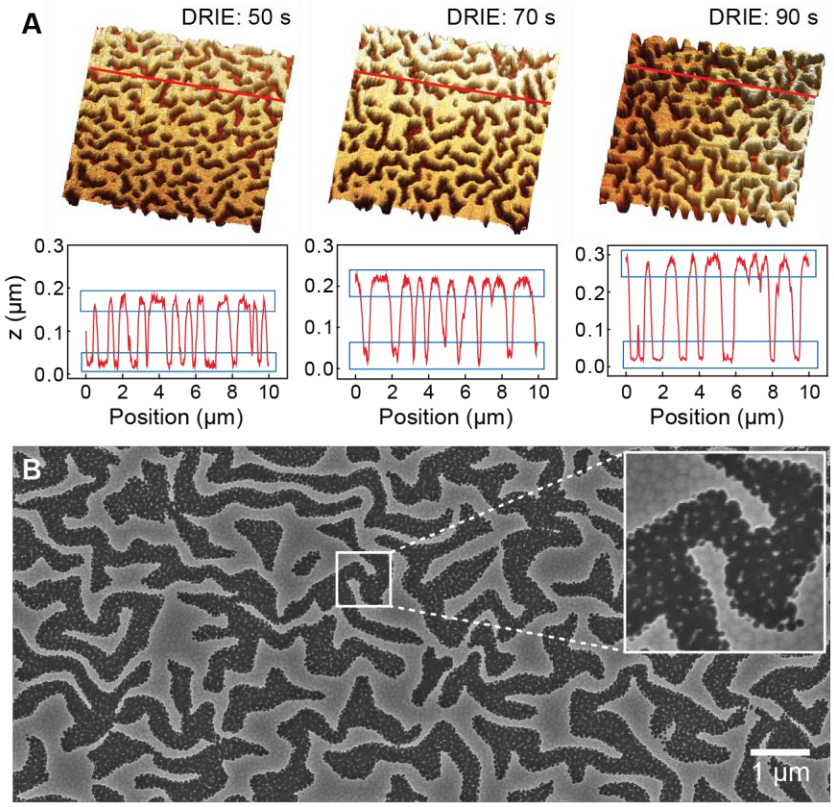

Fig. S13. Additional surface roughness on the quasi-random *a*-Si pattern. (A) AFM images of quasi-random patterns by wrinkle lithography and side profiles. Blue boxes show the additional surface roughness on the patterned structures. The additional roughness (RMS) was approximately 9 nm (DRIE time of 50s), 10 nm (DRIE time of 70s) and 10 nm (DRIE time of 90s). **(B)** SEM image showing the additional surface roughness on the bottom and the step edges of the patterns.

Supporting Information References

1. Huntington MD, Engel CJ, & Odom TW (2014) Controlling the orientation of nanowrinkles and nanofolds by patterning strain in a thin skin layer on a polymer substrate. *Angewandte Chemie International Edition* 53(31):8117-8121.
2. Lee W-K, Engel CJ, Huntington MD, Hu J, & Odom TW (2015) Controlled three-dimensional hierarchical structuring by memory-based, sequential wrinkling. *Nano Lett.* 15(8):5624-5629.
3. Huntington MD, Engel CJ, Hryn AJ, & Odom TW (2013) Polymer nanowrinkles with continuously tunable wavelengths. *ACS Applied Materials & Interfaces* 5(13):6438-6442.
4. Lee MH, Huntington MD, Zhou W, Yang J-C, & Odom TW (2011) Programmable soft lithography: Solvent-assisted nanoscale embossing. *Nano Lett.* 11(2):311-315.
5. Champeney DC (1987) *A handbook of Fourier theorems* (Cambridge University Press, Cambridge Cambridgeshire ; New York) pp ix, 185 p.
6. Torquato S (2002) Statistical description of microstructures. *Annu. Rev. Mater. Res.* 32:77-111.
7. Teubner M (1991) Level surfaces of Gaussian random-fields and microemulsions. *Europhys. Lett.* 14(5):403-408.
8. Goldberg DE (1989) *Genetic Algorithms in Search, Optimization, and Machine Learning* (Addison-Wesley Professional).
9. Yu S, Wang C, Sun C, & Chen W (2014) Topology optimization for light-trapping structure in solar cells. *Struct. Multidiscipl. Optim.* 50(3):367–382.
10. Wang C, Yu SC, Chen W, & Sun C (2013) Highly Efficient Light-Trapping Structure Design Inspired By Natural Evolution. *Scientific Reports* 3.
11. Martins ER*, et al.* (2013) Deterministic quasi-random nanostructures for photon control. *Nature communications* 4:2665.
12. Deb K & Beyer HG (2001) Self-adaptive genetic algorithms with simulated binary crossover. *Evol Comput* 9(2):197-221.
13. Pierce DT & Spicer WE (1972) Electronic Structure of Amorphous Si from Photoemission and Optical Studies. *Physical Review B* 5(8):3017-3029.
14. Li L (1997) New formulation of the Fourier modal method for crossed surface-relief gratings. *J. Opt. Soc. Am. A* 14(10):2758-2767.
15. Moharam MG, Gaylord TK, Grann EB, & Pommet DA (1995) Formulation for stable and efficient implementation of the rigorous coupled-wave analysis of binary gratings. *J. Opt. Soc. Am. A* 12(5):1068-1076.
16. Moharam MG & Gaylord TK (1982) Diffraction analysis of dielectric surface-relief gratings. *J. Opt. Soc. Am.* 72(10):1385-1392.
17. Xiong Y, Liu ZW, & Zhang X (2008) Projecting deep-subwavelength patterns from diffraction-limited masks using metal-dielectric multilayers. *Appl. Phys. Lett.* 93(11):111116.
18. Byun KM, Kim SJ, & Kim D (2005) Design study of highly sensitive nanowire-enhanced surface plasmon resonance biosensors using rigorous coupled wave analysis. *Opt. Express* 13(10):3737-3742.
19. Li L (1996) Formulation and comparison of two recursive matrix algorithms for modeling layered diffraction gratings. *J. Opt. Soc. Am. A* 13(5):1024-1035.

20. van Lare MC & Polman A (2015) Optimized Scattering Power Spectral Density of Photovoltaic Light-Trapping Patterns. *ACS Photonics* 2(7):822-831.
21. Yu Z, Raman A, & Fan S (2010) Fundamental limit of nanophotonic light trapping in solar cells. *Proc. Natl. Acad. Sci. U.S.A.* 107(41):17491-17496.
22. Yablonovitch E (1982) Statistical ray optics. *J. Opt. Soc. Am.* 72(7):899-907.